J. Fluid Mech. (1986), *vol.* 165, *pp.* 247–272
Printed in Great Britain

The generation of circulation and lift in a rigid two-dimensional fling

By G. R. SPEDDING AND T. MAXWORTHY

Department of Aerospace Engineering, University of Southern California, Los Angeles, California 90089-0192

(Received 1 August 1985)

The instantaneous lift forces on a pair of rigid wings opening by rotation about a common trailing edge (the fling) are measured and related to the unsteady flow field as revealed by simultaneous flow visualization. The effect of altering the wing-opening time history and the initial opening angle of the wing pair on circulation and lift generation is investigated. Dimensionless circulations and lift coefficients are compared with experimental and theoretical results in the literature and the relevance of these results to insects and engineers is discussed.

1. Introduction

Since its original formulation by Weis-Fogh (1973) and Lighthill (1973), the clap-and-fling mechanism of enhanced lift generation has attracted attention not only as an interesting problem in unsteady fluid mechanics but also as one with potentially significant practical ramifications. The basic motion (figure 1) is two-dimensional in an inviscid fluid. Two wing sections are shown clapped together with the wing chords parallel and vertical. The two surfaces are then pulled apart by rotation about the common trailing edge at an angular velocity $\Omega = \mathrm{d}\alpha/\mathrm{d}t$, where α is the opening half-angle between the wing pair (figure 1*b*). This rotation continues until some value α_c, typically assumed to be $\frac{1}{3}\pi$ rad (figure 1*c*), when the wing sections move apart in translation at velocity U (figure 1*d*). Air flowing into the opening gap during the rotating (or fling) phase creates equal and opposite circulations of magnitude Γ around each wing without violation of Kelvin's theorem as the total circulation around the wing pair remains zero. When the wings part, each immediately experiences a lift $L = \rho\Gamma U$, where ρ is the fluid density, without the delay associated with vortex shedding in the classical problem of an impulsively started aerofoil (Wagner 1925). According to inviscid theory, $\Gamma = 0.69\Omega c^2$ at $\alpha = \frac{1}{3}\pi$, for wings of chord c.

Maxworthy (1979) confirmed the basic premises of this scheme but also demonstrated the importance of viscous effects in the form of large leading-edge separation vortices whose circulation continued to increase until $\alpha \approx 150°$ when $\Gamma \approx 6\bar{\Omega}c^2$. Similar results were reported for flow Reynolds numbers, $Re = \bar{\Omega}c^2/\nu$ ($\bar{\Omega}$ is the mean angular velocity, ν the kinematic viscosity of the fluid), of 32 and 1.3×10^4. The presence of large separation vortices is also shown by the instantaneous streamlines and iso-vorticity lines computed by Haussling (1979) who solved the full Navier–Stokes equations on a coordinate mesh fitted to the moving solid boundaries at $Re = 30$. More recently, Edwards & Cheng (1982) applied an inviscid analysis but with a concentrated vortex whose circulation is increased by the addition of vorticity shed at the leading edge. A force-free condition on the vortex and its feeder sheet was used to determine

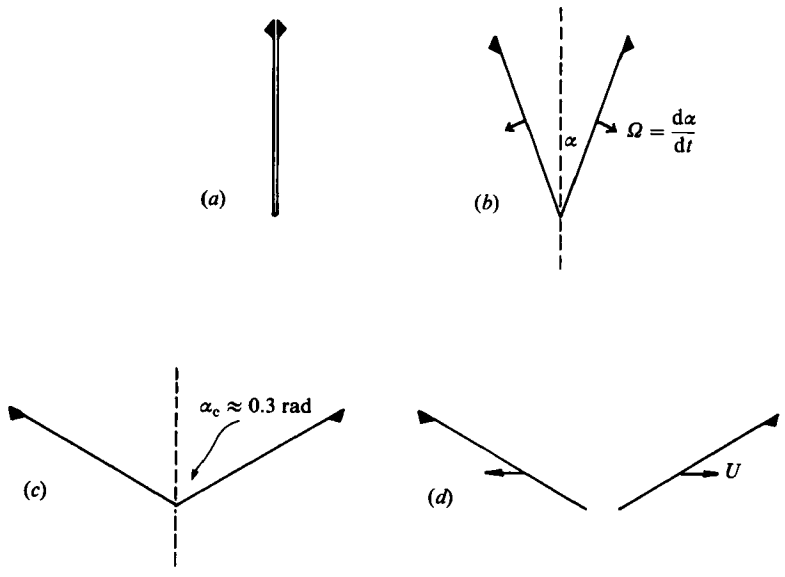

FIGURE 1. The two-dimensional fling.

the location and strength of the vortex. The calculated Γ increased over the range $0.26 < \alpha < \frac{1}{2}\pi$ rad, in general agreement with Maxworthy's experimental results. Wu & Hu-Chen (1984) have also formulated a vortex-separation model where a constant radial location of the vortex at c (chord length) was assumed, its strength being determined by the rate of generation of vorticity at the leading edge, and the angular location was given by imposing a Kutta condition at the leading edge. Γ estimates from this model were very close to those of Edwards & Cheng and predictions of lift and power requirements were also given.

The applications of the clap and fling in two- and three-dimensional analyses of insect flight have been considered by Maxworthy (1981) and Ellington (1975, 1980, 1984) who also discussed the possible effects of a 'near' or 'partial' clap and fling together with modifications due to wing flexibility. Scholey (1982) has filmed a wide range of birds in take-off or landing manoeuvres where the operation of a 'near' clap-and-fling motion is implicated.

The basic processes involved in the fling mechanism, which may be formulated in a purely two-dimensional, inviscid framework, are of great interest in problems involving unsteady flows around deformable or multiple bodies. Furber & Ffowcs Williams (1979) proposed a design for an axial-flow compressor based on increasing unsteady effects due to rotor–stator interaction. Potential-flow calculations showed a higher stage loading under a wide range of operating conditions and preliminary experiments indicated significant performance advantages from increased blade interaction. From an aerodynamics standpoint, there is continued interest in the generation and entrapment of unsteady vortex flows for lift enhancement on the wings of super-manoeuvrable aircraft (e.g. Rossow 1978). The clear understanding of the fluid dynamics of fling-type motions is of fundamental importance to this effort.

In this paper we elaborate on the previous work of Maxworthy (1979) and present results of the measurement of instantaneous forces of an opening wing pair, and relate these to the unsteady flow field of a two-dimensional rigid fling motion. The effects of changing the initial opening angle α_0 and the wing angular velocity Ω are also investigated.

2. Materials and methods

2.1. *Mechanical models*

Figure 2 is a schematic of the apparatus in side and front elevation. A $0.7 \times 0.8 \times 0.8$ m Plexiglas tank is capped by an anodized-aluminium collar and top plate, on top of which are mounted two support towers (t) for attachment of the load cells (lc). Two 10 mm thick Plexiglas end plates (ep) between which the wings operate are also fixed in the laboratory frame of reference, which is denoted by cross-hatching in the schematic. The wings (w) are constructed from 6 mm Plexiglas with chord $c = 10$ cm and length $s = 30$ cm, and taper to a sharp leading edge from $0.8c$. The wings are driven by weights pulling around four pairs of counter-rotating pulleys (P_{1-4}) and are connected via vertical push rods (r) to two strain-gauge load-cells which have an adjustable coupling to the outer frame. The weights used were old plastic film canisters to which accurately pipetted volumes of water could be added.

2.1.1. *Procedure*

In each series of experiments, the tank was filled with water, flexible tubing allowing air to escape from the floats (f) attached to each push rod. Air was then slowly pumped into the floats until the wing assembly became neutrally buoyant. At this point the load cells were fastened to the support towers and any vertical forces experienced by the wing assembly were thus transmitted directly to the load cells. The only vertical motion possible was that of the load-cell elements themselves and was negligible. The load cells were calibrated in a loading and unloading cycle, gradually increasing and decreasing the weight applied by an arrangement of pulleys to the mid-point of the wing support shafts. The force range of interest could be covered in about 20 min. Dynamic response was checked by applying a series of step-function type inputs of half full-scale. The calibration cable attachment was then replaced by the wing release catch, which was triggered either manually or by computer-controlled relay. During each run, the wings opened once, and were subsequently raised manually.

2.1.2. *Flow visualization*

Two flow-visualization techniques were employed; the first involved small polystyrene beads with a diameter ≈ 0.75 mm and specific gravity ≈ 1.035. Salt was added to the tank to bring the water density to about 1.03 and a vertical light slice at the mid-plane of the wings was provided by 2 kW lights. Immediately before each run, beads were introduced at the water surface in the light plane, and a curtain of beads would drift downwards at speeds of the order of 2–3 mm s^{-1}. Beads were added continuously until the curtain reached the bottom of the tank. The wing release was triggered about 10 s later (after enough time for all abnormally heavy particles to have sunk) and time-exposure photographs recorded particle paths. For the second visualization technique, which revealed smaller-scale fluid motion, a suspension of aluminium dust was added to fresh water and illuminated with the same light slice. Although they trace out small details of the flow, these particles cannot be confidently used for quantitative measurements owing to their lamellar shape, as discussed by Maxworthy (1971) and Heikes & Maxworthy (1982), and recently by Savaş (1985).

2.1.3. *Instrumentation*

The load cells (Sensotec Inc., Model no. 31/235) are sensitive to compression and tension over a range of ± 500 g with 0.2% linearity and hysteresis over the entire

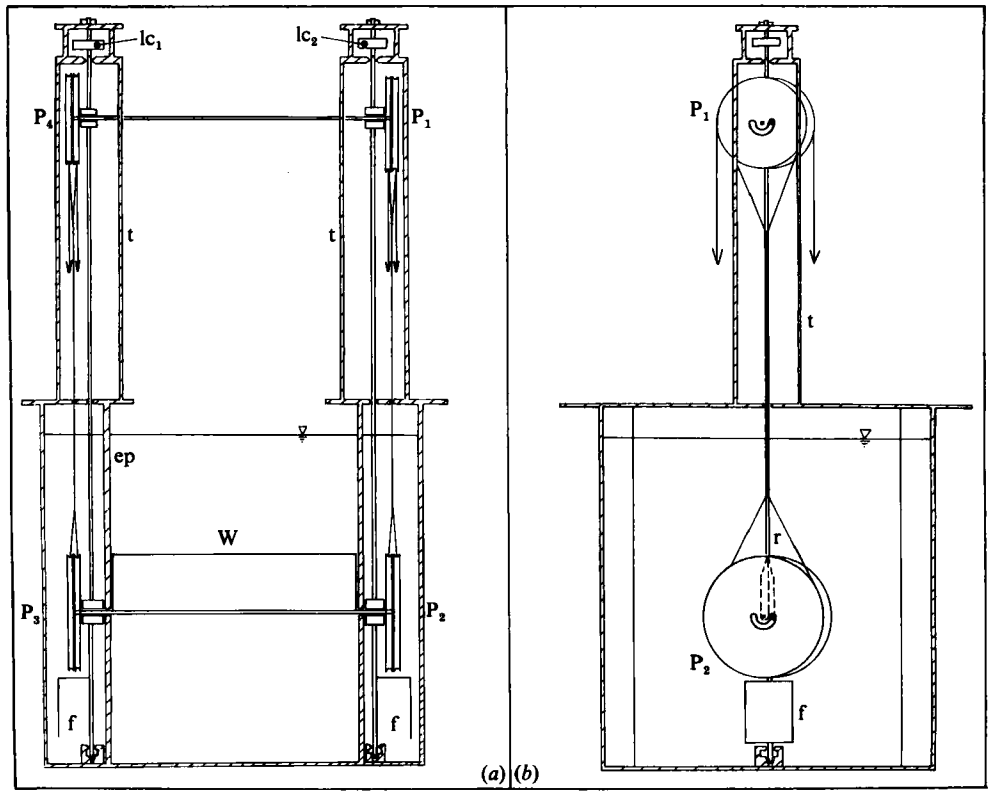

FIGURE 2. Side (*a*) and front (*b*) views of apparatus. Not to scale.

range. Bridge excitation at 6.0 V and signal amplification to ± 10 V f.s.r. were provided by an SCA-7 Amplifier (also Sensotec Inc.).

The wing position was monitored by recording the output of an infra-red phototransistor/l.e.d. pair placed either side of a calibrated disk attached to one of the upper drive pulleys. The disk was constructed by making a Lith positive print of a circle whose perimeter was divided into 92 alternately light and dark segments. Each light-to-dark transition occurs with a disk rotation of 3.91°/0.0683 rad and was detected at the mid-point of a jump in signal voltage from 0–5 V. Due to the relative sizes of the upper and lower pulleys, each step was equivalent to 2.81°/0.049 rad of wing rotation.

For data acquisition and experimental control two Cromenco Z-2 microcomputers were linked in a master–slave configuration, the master (C1) including 64 K RAM and a 16 channel, 12-bit a.d.c. module. C1 recorded data from the load cells and wing-position disk and initiated execution of programs in C2. C2 (32 K RAM) could store and execute from RAM programs sent from C1 and also contained several customized programs in ROM for running stepping motors, operating the cameras and triggering the wing release mechanism. Both control and input functions of some complexity could thus be realized in real time.

35 mm cameras were used for recording particle traces, either a Nikon F2 or F3 with 55 or 135 mm Nikkor lenses. The camera was aligned centrally and normally to the light slice by sighting with its reflection in the front face of the Plexiglas tank, and checking its level with a spirit level. Photographs were digitized on a Houston Instruments Hipad digitizing tablet connected to C1.

2.2. *Data reduction and analysis*

All data were transferred over a phone line to a PDP11/55 minicomputer where all calculations were performed.

Flow-visualization data were treated as follows: from each photograph 4000–5000 coordinate pairs were taken by manually marking the beginning and end of particle streaks. In this case, the direction of flow was easily judged, ambiguous points were simply ignored and some care was taken to ensure a reasonable density of data near 'interesting' points in the flow, such as regions of high shear; at present such procedures resist simple automation. Each streak yields u and v velocity components at a point (x, y). The velocity field was reduced by linear least-squares interpolation to a 30×30 square mesh grid from the relations

$$u_n = u + \frac{\partial u}{\partial x} x_n + \frac{\partial u}{\partial y} y_n, \tag{1}$$

$$v_n = v + \frac{\partial v}{\partial x} x_n + \frac{\partial v}{\partial y} y_n, \tag{2}$$

where, at each mesh point, the unknown velocities u and v and their derivatives in x and y were interpolated from all data points (x_n, y_n, u_n, v_n) within the neighbourhood of that mesh point. This procedure is similar to that described by Imaichi & Ohmi (1983). Other quantities of interest such as the vorticity

$$\omega = \frac{\partial v}{\partial x} - \frac{\partial u}{\partial y} \tag{3}$$

are easily calculated at all mesh points. On occasion the interpolation would fail, giving a highly improbable result, in which case mesh points showing excessive velocity fluctuations were replaced by a mean of neighbouring values. The circulation of the separation vortex

$$\Gamma = \oint \boldsymbol{u} \cdot \mathrm{d}\boldsymbol{x} \tag{4}$$

was calculated by integrating around streamlines which formed a closed curve. This was performed in an interactive graphics operation by specifying a starting mesh point, following and tracing out a streamline and integrating around the loop if it closed. At the mesh borders the integral path travels around the edge and is forced to return down the centreline when and if it is reached. The measured value of Γ turned out to be relatively insensitive to the location and length of the integral path, provided that it lies outside the vortex core.

Load-cell and wing-position data were generally taken at 5 ms intervals for 10 s. No attempt was made to minimize the number of data points, as limits on RAM or disk storage space posed no problem. The raw load-cell data were zeroed, brief transients caused by operation of the wing release mechanism (conveniently marking a starting point) removed, and then scaled. Each channel was then sent through a low-pass FIR digital filter (McClellan, Parks & Rabiner 1973) after which the mean of both channels was calculated and retained. The square-wave trace of wing position vs. time was converted to angular position (given the initial opening angle) and the moment applied to the wing roots was calculated from this information together with the initial geometry of the pulley-and-cable drive mechanism. Each applied moment and angular-position point corresponds to a particular time when a local least-squares polynomial fit was made to find the corresponding lift force. In combining different

runs for identical conditions, a standard data set was produced by expanding the time data to 128 points and finding the force, angular-position and applied-moment data with a smoothing or interpolating spline approximation as appropriate (Dierckx 1975). All of the data plots given below are composed of straight-line segments through this data.

3. Measurement accuracy and sources of error

The photogrammetric requirements were not stringent in this case and the photography and reconstruction of a plane square grid indicated that camera misalignment, lens distortion, film shrinkage and contouring and digitizing-pad resolution (0.13 mm) could be ignored as sources of serious error. In fact the most obvious source of error is the pointing error in marking streak positions, as each particle has a finite diameter which must be estimated by the operator in locating the beginning and end of each streak. With small velocities or short streaks, the relative magnitude of this error increases and could be one cause of the odd 'blow-up' of the least-squares interpolation as previously noted. Apart from such catastrophic cases, which were corrected as previously described, it was noted that two independent digitizations, by different operators, of the same photograph produced differences in Γ, for example, of 8% or less.

The error due to the finite response time of the camera shutter is small relative to the exposure time and may be checked by removing the lens and photographing the shutter motion during a typical exposure (0.25 s) with a second identical camera at much higher shutter speeds (0.001 s). The estimated frame error (< 0.05 s) was low enough to be ignored; so too was the difference in specific gravity of the polystyrene beads and the surrounding fluid (1.037–1.030).

The resolution of the load cells and a.d.c.'s (0.2% and 12-bit, respectively) were entirely adequate even when operating over only half of the full scale range for some safety margin. Load-cell calibration showed some hysteresis in both the static (15% worst case) and dynamic tests, the latter displaying signs of viscoelastic-type behaviour. Typically, however, 96% response was reached in 0.22 s and 99% in 0.55 s in positive and negative step-loading tests. Calibration was repeated before each series of experiments and checked to be satisfactory before continuing.

Some considerations regarding the fidelity of the model should also be noted. Although the wing pair operated between two end plates to enforce a two-dimensional flow, some inflow might be expected around the gap between them. Figure 3 shows the extent of this crossflow during the initial stages of wing opening ($\alpha = 17°$) when the fluid velocity and acceleration round the wing are high. Crossflow at the wing roots through the slotted and end plates was prevented by sliding thin plastic plates along the wing support shafts until they lay flush with the outside surface of the end plates; the fluid pressures developed during the experiment tend to keep them there.

4. Flow-visualization results

In the first version of the apparatus, a stepping motor opened the wings directly through a gear box mounted on the outer wall of one wing end plate. In that case, the wing-opening time history could be prescribed while in the present version one specifies, through the geometry and arrrangement of the pulleys and cables and the mass of the weights, the moment applied at the wing root throughout the wing-opening cycle. Although stepping motors were eventually discarded due to excessive noise,

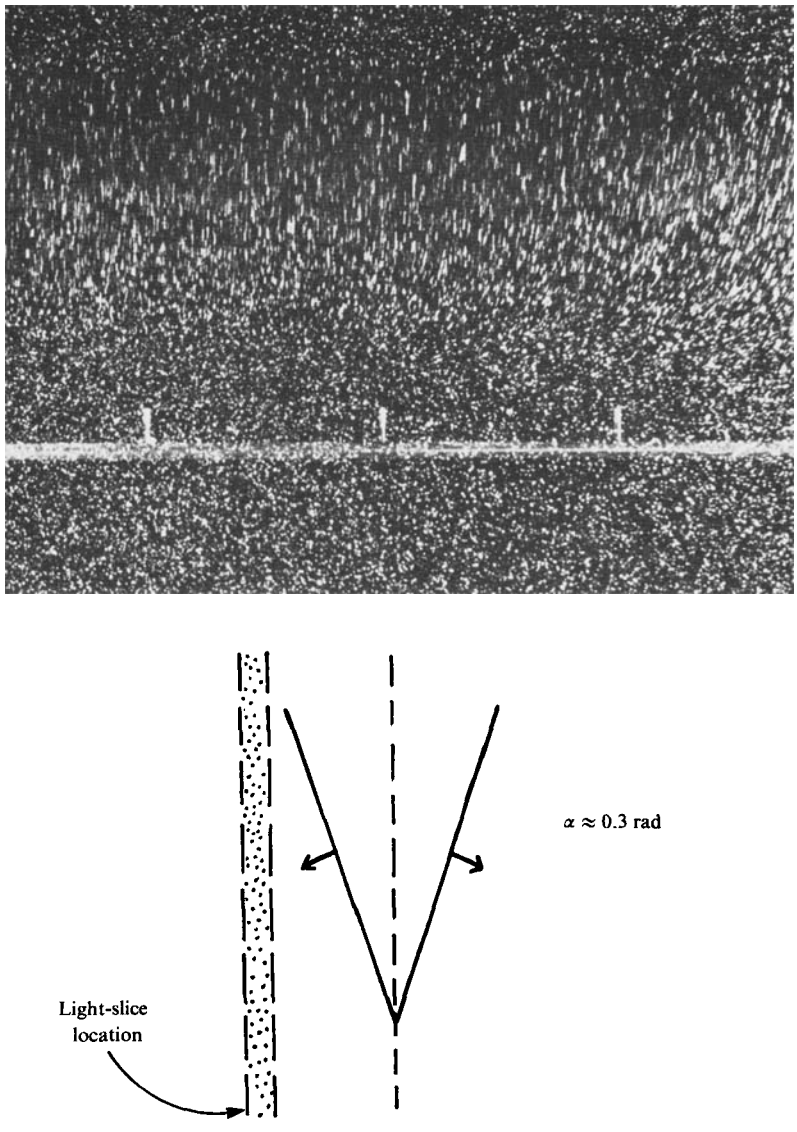

FIGURE 3. Light slice parallel to wing axis shows departure from two-dimensional flow. Aluminium-dust suspension, exposure time $e = 0.25$.

dynamic imbalance, resonance at low operating speeds and impulsive initial torque application, the flow-visualization experiments performed with this configuration revealed interesting details of the flow and also of the visualization techniques themselves. Two different wing-opening time histories are compared in figure 4. In C3 the wing angular velocity is constant while F3 accelerates smoothly from rest to a constant Ω. Figure 5 is a series of polystyrene-bead streak photographs taken at constant time intervals during one wing-opening cycle. The overall flow field, dominated by separation vortices shed at the leading edges, is much as described by Maxworthy (1979, 1981).

Initially, the flow is asymmetric about the midline. Then a secondary recirculation develops within one of the vortices which elongates and covers a larger fraction of

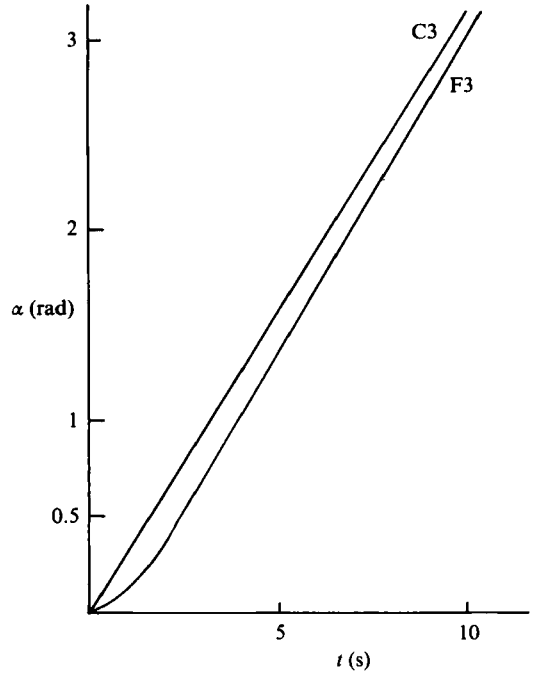

FIGURE 4. Wing-opening time histories $\alpha(t)$ for cases C3 ($\Omega = 0.36$ rad s^{-1}) and F3.

the wing chord than its opposite partner (figure 5(*b*)). This region grows no further however and is obliterated during development of the tip-separation vortex and the flow later appears symmetric about the two wings (figure 5*e*). We also note that at no time is the vortex core circular in shape: it is always slightly elliptic with the long axis parallel to the wing chord, and further distortion is apparent towards the end of the wing stroke (figures 5*i–l*). This distortion of the vortex-core shape is more apparent at lower Reynolds numbers (cf. Maxworthy 1979); here $Re = 3 \times 10^3$. This flow is for a constant Ω and close inspection of the streak photographs reveals the flow in the core to be turbulent at all times. Criss-crossing particle paths may also be found immediately above the wings in figures 5*b–i*. The extent of the turbulence is clear from figure 6, which is a series of aluminium-dust visualizations for identical conditions. Darker areas in these photographs correspond to regions of high shear and, in the first 9 or 10 frames, outline the edges of the separation vortices. Within these areas the flow appears quite disorganized while the turbulent regions on the wing surface appear to have a roll-like structure running transversely across the wing pair for opening angles $60° \lesssim \alpha \lesssim 120°$. In order to investigate the extent to which the flow has developed organized three-dimensional structures, the experiment was repeated with a vertical light slice running parallel to the wing roots and displaced laterally from them by $\frac{1}{2}c$ (figure 7). These photographs show substantial departures from two-dimensional flow in the turbulent core regions and some vortex patterns persist over the 50° of wing opening shown here.

The flow pattern for the F3 case, by contrast, is almost entirely laminar and very similar to the photographs already published by Maxworthy for $Re = 1.3 \times 10^4$. Turbulence within the core region is much reduced, and is absent immediately above the wing surface. Vorticity shed at the leading edge convects directly into the

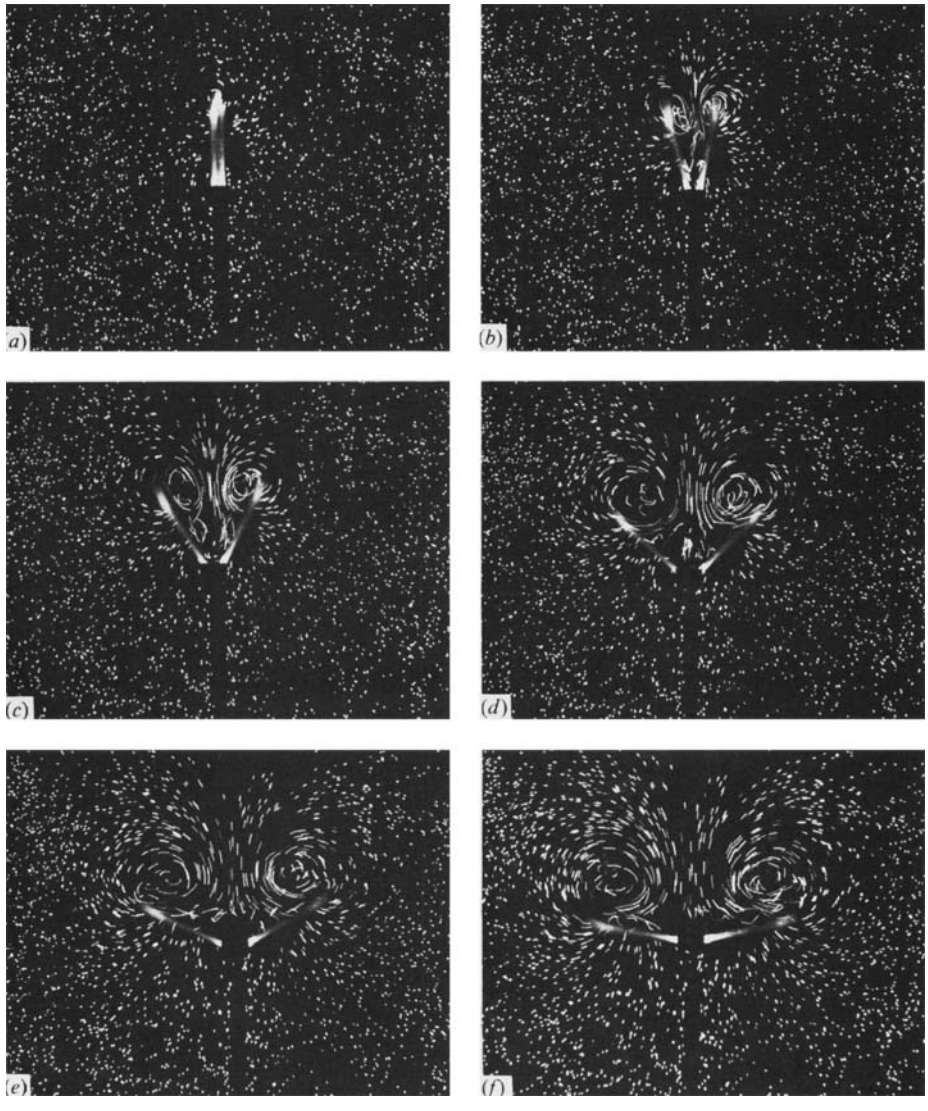

FIGURE 5(*a–f*). For caption see next page.

separation vortices without contamination from a turbulent region above the wing.

One might expect these differing flow fields to affect the strength of the separation vortices and figure 8 shows this to be the case. The circulation was measured from the interpolated velocity fields of digitized photographs and averaged for all integration paths covered as shown in figure 9. The normalized circulation shows reasonable agreement with previous results and the effect of the wing-opening time history is obvious. In the impulsively started case (C3), Γ grows slowly, if at all, when figures 5–7 indicate the presence of a turbulent region above the wings. In the F3 case, the circulation continues to rise throughout the wing-opening cycle, reaching values of about $6\bar{\Omega}c^2$ at $\alpha = \pi$ rad. These differing circulations should also have a measurable effect on the forces experienced by the wings.

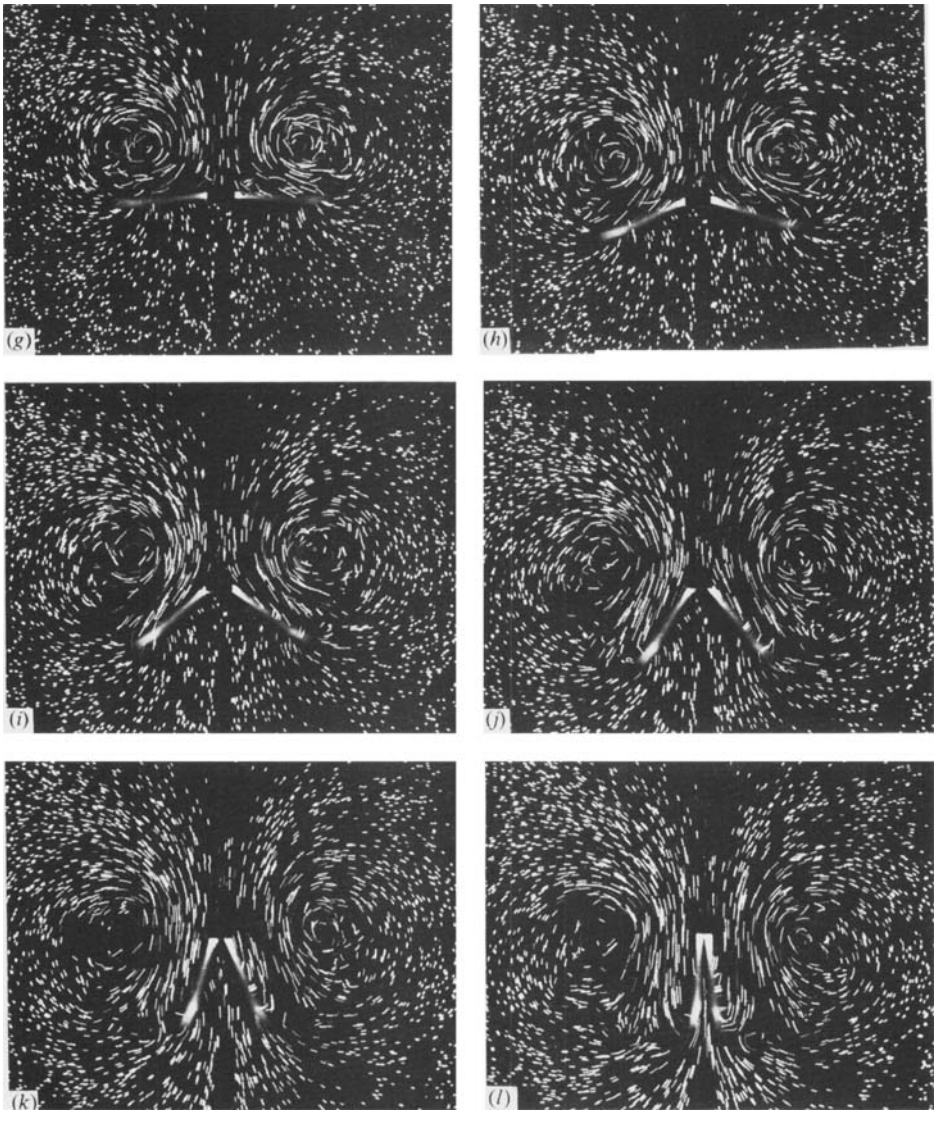

FIGURE 5. Time series of streak photographs for case C3 from $\alpha = 0$ to $\alpha = \pi$ rad. Time between successive photographs = 0.8 s, $e = 0.25$ s. Particles are polystyrene beads.

5. Lift measurements

Figure 10 shows the output from one load cell as the wings open from $\alpha \approx 0$ to $\alpha = \frac{1}{2}\pi$ rad. The moments of wing release and closure are marked by sharp transients which give some idea of the response time of the system. The lift force, given in arbitrary a.d.c. units (resolution 1 unit) is positive throughout the wingstroke with magnitude and frequency very different from electrical and mechanical noise. The wings move only imperceptibly immediately after release as viscous forces resist separation of the two close surfaces, so there is some delay before the lift curve rises. It remains high until the wings close and in these latter stages will include a

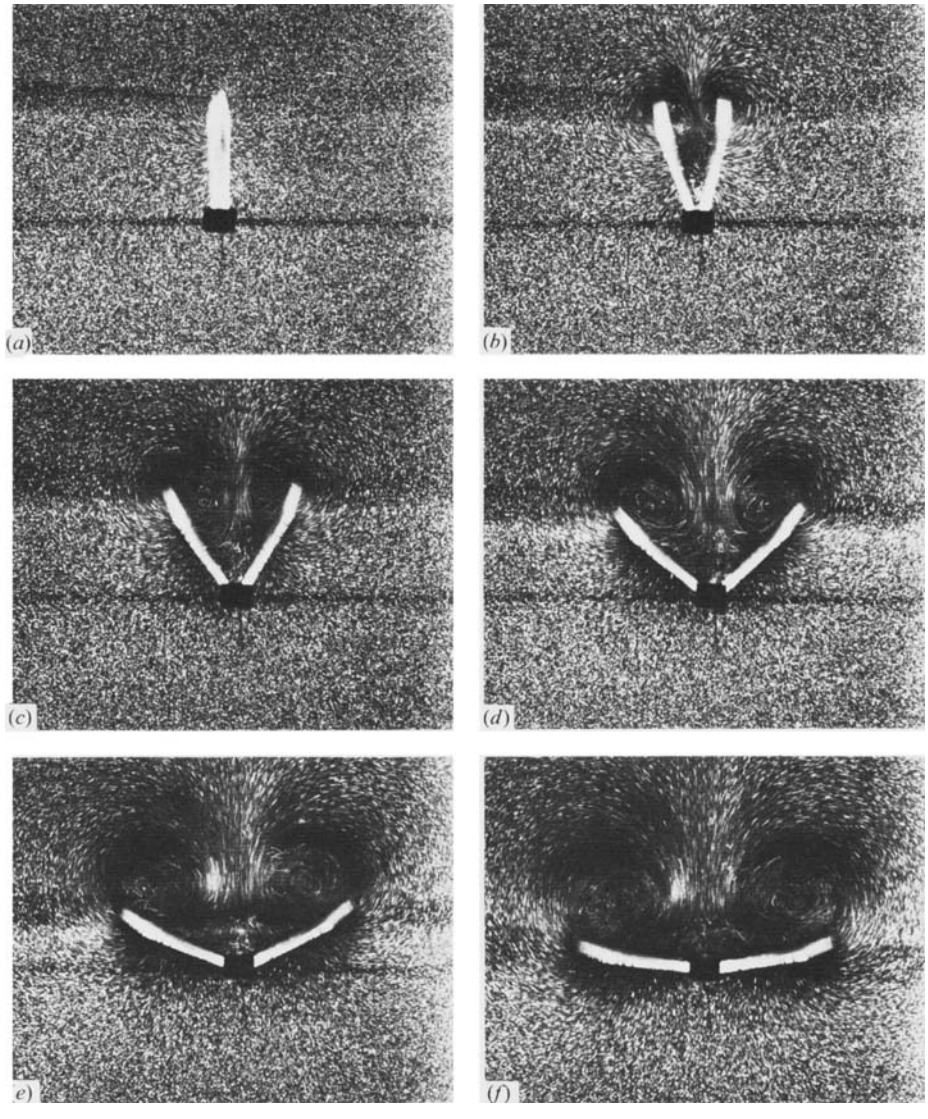

FIGURE 6 (*a–f*). For caption see next page.

contribution from the jet of fluid pushed out from between the closing wings.† Afterwards, the small negative lift is presumably due to skin friction and form drag of the wing pair in the induced flow between the vortex pair, and the low-amplitude oscillations occur at the natural frequency of the tank.

† Vertical accelerations of the weights are small and have been ignored. When each weight has mass 60 g, the total weight is 1.18 N. If the weights drop ≈ 0.6 m in 3.7 s, their mean vertical velocity is 0.16 m s^{-1}. Suppose a maximum acceleration of 0.2 m s^{-2} (high), then the force would be 0.24 N. Under these conditions a peak force of 4.27 N was measured, with a mean of 2.03 N over the wingstroke. Similar considerations apply to the acceleration of the wings themselves which also have some weight w in water. The lift force would be $L_w = wr\dot{\Omega}\sin\alpha$, where $\dot{\Omega}$ is the angular acceleration of the wings at position α, and r is the chordwise location of the centre of mass of the wings. We note that $\dot{\Omega}$ is generally small and largest when $\sin\alpha$ is small.

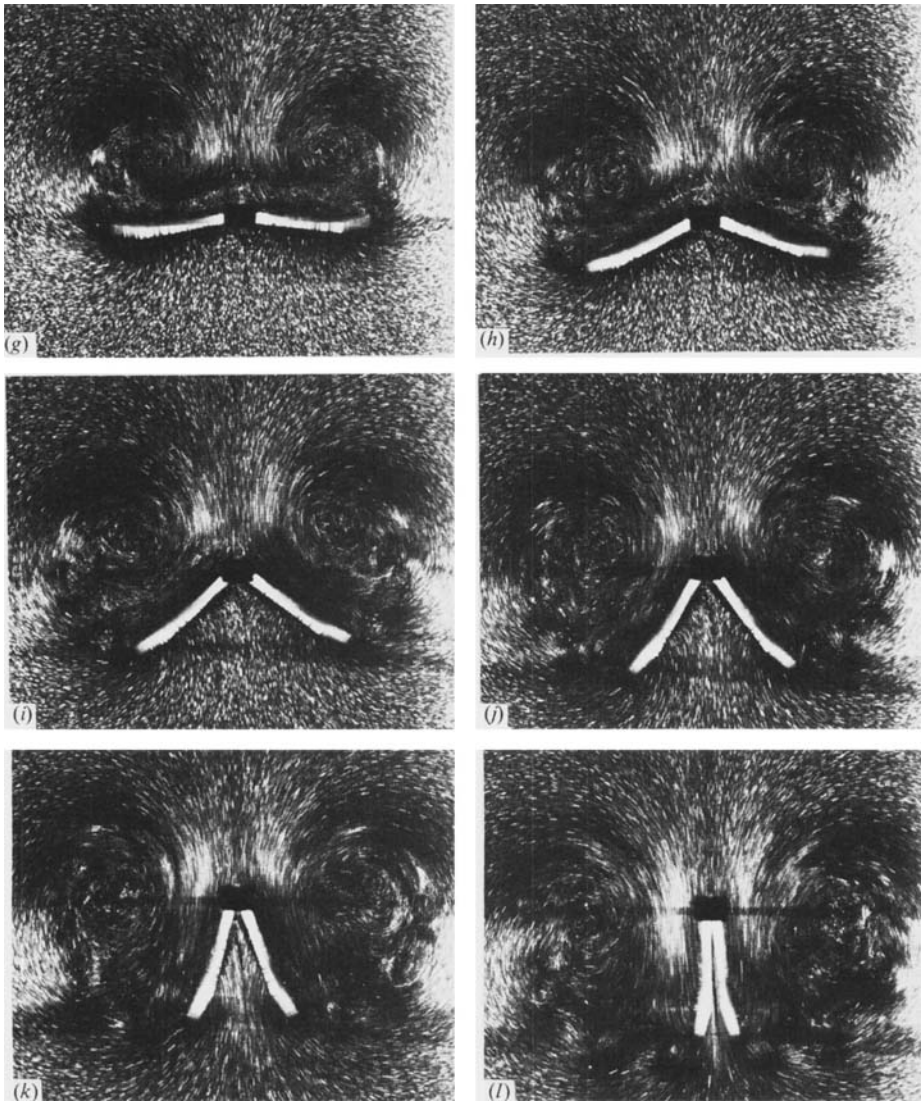

FIGURE 6. As figure 5 but with aluminium-dust suspension.

The mean moment $\overline{M}$ applied at the wing root may be changed by adding or subtracting water from the four weights. Figuress 11 (a,b) show the $L(t)$ and $L(\alpha)$ traces resulting from the $M(t)$ and $\alpha(t)$ histories of figures 11 (c,d). With decreasing $\overline{M}$ (traces 1–6), the maximum and total integrated lift force decreases while the time taken for the wings to open increases. Trace 6 rises more rapidly in figure 11 (a) as the wings had to start at some small initial opening angle α_0 in order to open at all, at these small values of $\overline{M}$. The $L(\alpha)$ curves are self-similar in α with $L_{\max}$ occurring at $\alpha = \frac{1}{2}\pi$, or just after.

The effect of varying α_0 is investigated in figures 12 (a,b) which show $L(t)$ and $\alpha(t)$ traces for α_0 varying from 0.49×10^{-2} to 0.21 rad. Differences in $L_{\max}$ are very small, even for the largest α_0 considered, and the chief effect of increasing α_0 is to decrease the total wing opening time T. Traces (i)–(iii) even show a small decrease in $L_{\max}$

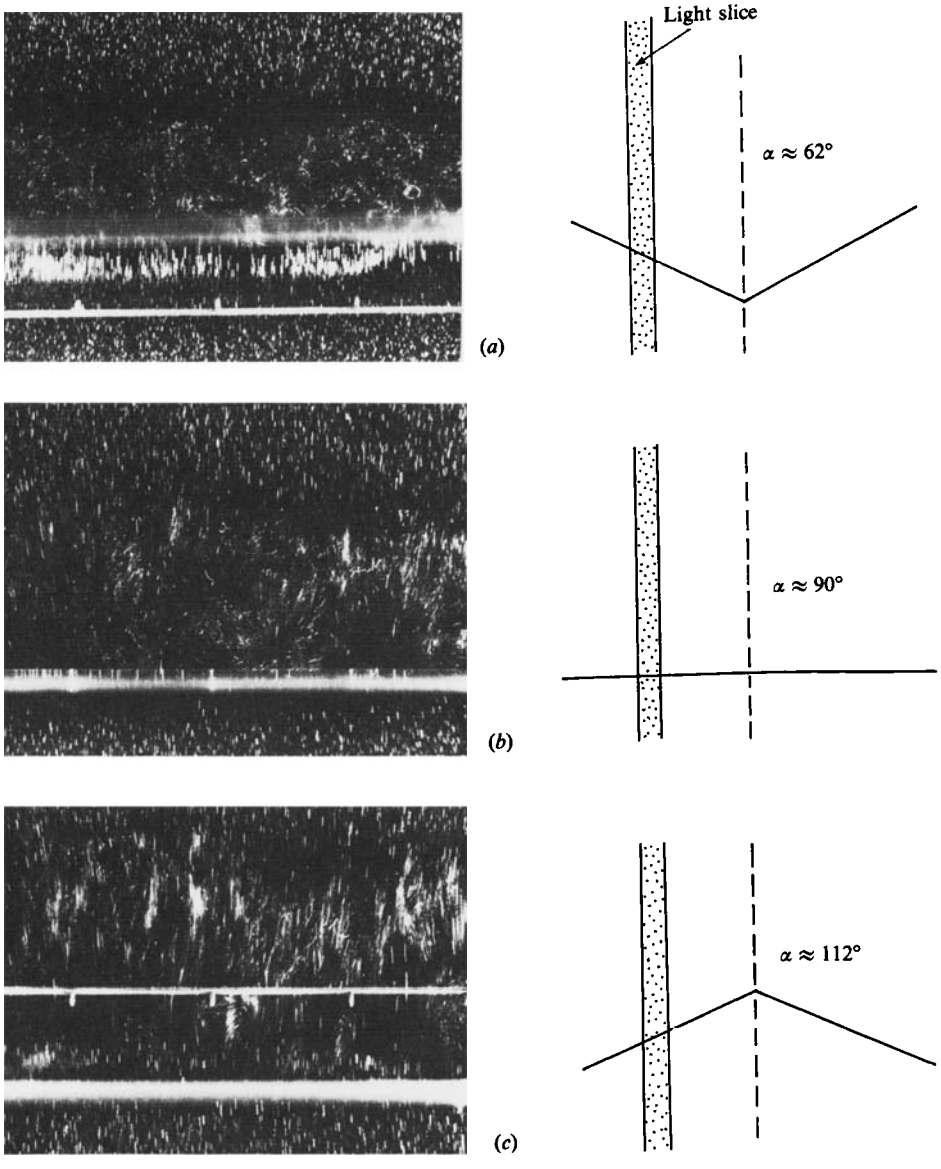

FIGURE 7. Light slice parallel to the wing pair. Experimental conditions as for figures 5 and 6.

with decreasing α_0. Each curve represents an average of 2–3 experiments and the time-aliasing error increases with small α_0 when combining experimental results by time. This is clear from figure 13, which shows $L(t)$ for eight single experiments for $\alpha_0 \approx 0$. Very small differences in α_0 lead to significant changes in T, but practically no difference in the shape of the $L(t)$ curve, once it begins. The three traces which fortuitously start to rise at the same time give some idea of the experimental scatter for (nearly) identical initial conditions.

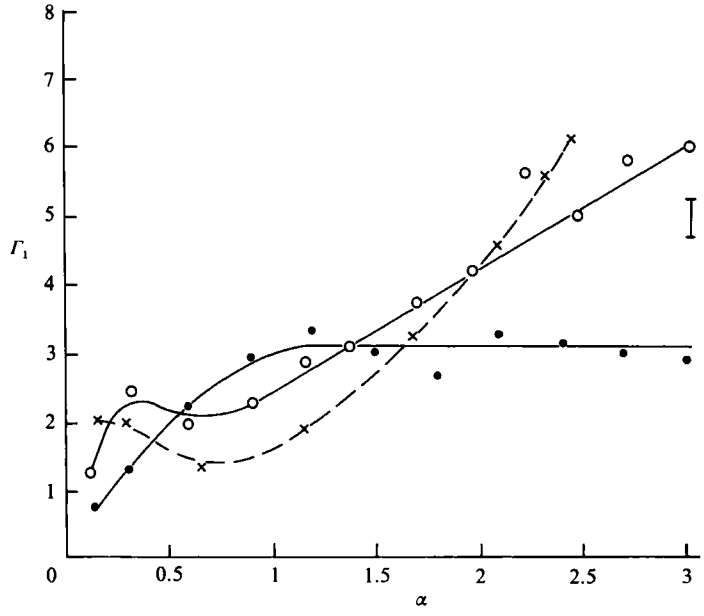

FIGURE 8. Dimensionless circulations, normalized by the mean angular velocity, for cases C3 (●—●), F3 (○—○) and results from Maxworthy's high-Re (1.3×10^4) case (×—×). $\Gamma_1 = \Gamma/\bar{\Omega}c^2$.

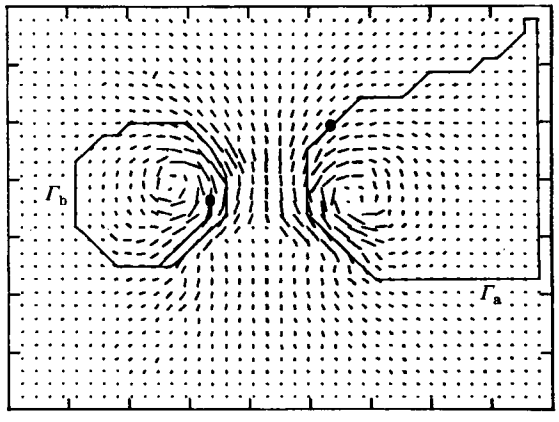

FIGURE 9. Integration round closed streamlines in interpolated velocity field. Starting points are shown by blobs. $\Gamma_a = 197$ cm^2 s^{-1}; $\Gamma_b = 178$ cm^2 s^{-1}.

6. Discussion

6.1. *Wing-opening time history*

The particular importance of $\dot{\Omega}$ in the initial stages of wing opening is shown by the flow-visualization experiments. By forcing a constant Ω over the whole opening cycle, or a very high initial $\dot{\Omega}$, the flow into the opening 'V' becomes turbulent, eventually spreading to cover by $\alpha \approx \frac{1}{2}\pi$ the entire wing surface. This turbulent fluid is also convected into the core regions of the separation vortices, which develop much lower circulations than in the corresponding laminar case (figure 9). It should be noted, however, that this flow could only be produced by the high torque available from

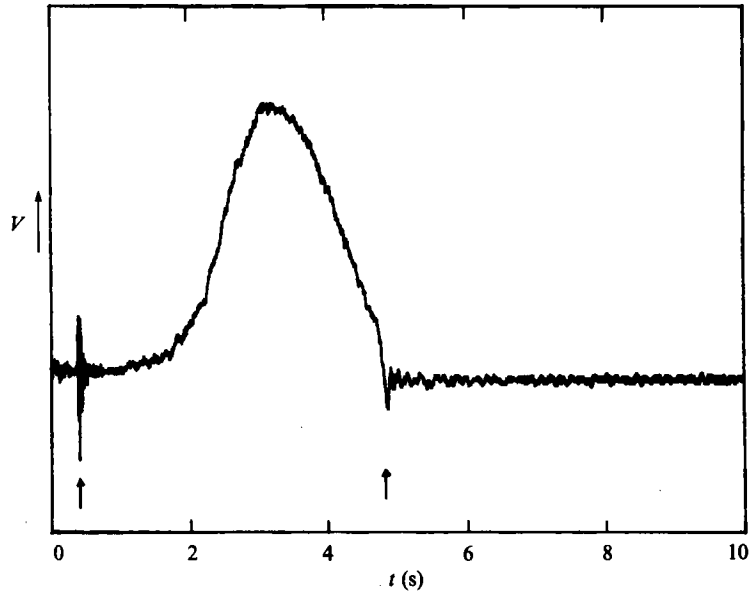

FIGURE 10. Untreated raw data from one load cell. Signal-to-noise ratio is low.

the stepping motors and any feedback loop of fluid-dynamic forces affecting the wing motion is broken. In most realistic cases, including all other experiments reported here, viscous forces and pressure gradients in the flow field moderate the initial values of $\dot{\Omega}$ and are responsible for the shape of $\alpha(t)$ for a given mean applied moment $\overline{M}$. Such is the case for all the force-measurement experiments which have a smooth opening curve. Although $\overline{\Omega}$ in these experiments is typically 2–3 times that of the constant-Ω case (C3), the flow above the wings always remained laminar.

This result may be of some significance in attempts at vortex trapping by wing-leading-edge flaps although the addition of a mean flow may alter this. It may also be noted that, while the effect on the flow field can be seen early on, the change in Γ is most noticeable for $\alpha > \frac{1}{2}\pi$, beyond the likely range of flap operation. The question is probably academic as far as the animal kingdom is concerned as few flying animals are likely to carry around a drive system able to deliver the excess torque required for an impulsive fling.

6.2. *Circulation and lift*

The Weis-Fogh mechanism is usually discussed as a means of developing high circulations around an opening wing pair before their subsequent separation and translation. We have shown here that the two-dimensional fling motion itself is capable of producing large values of L, as might be expected from inspection of the flow-visualization results. Correspondence between the direct lift measurements and digitized particle-streak data may be tested by comparing the total impulse estimated in each case. The impulse is

$$I = \int_0^T \boldsymbol{F}(t)\,\mathrm{d}t, \tag{5}$$

and is estimated from $L(t)$ records such as in figure 11 (*a*). The wings open at $t = 0$ and close at $t = T$. If the flow field at $t = T$ is modelled as a pair of point vortices

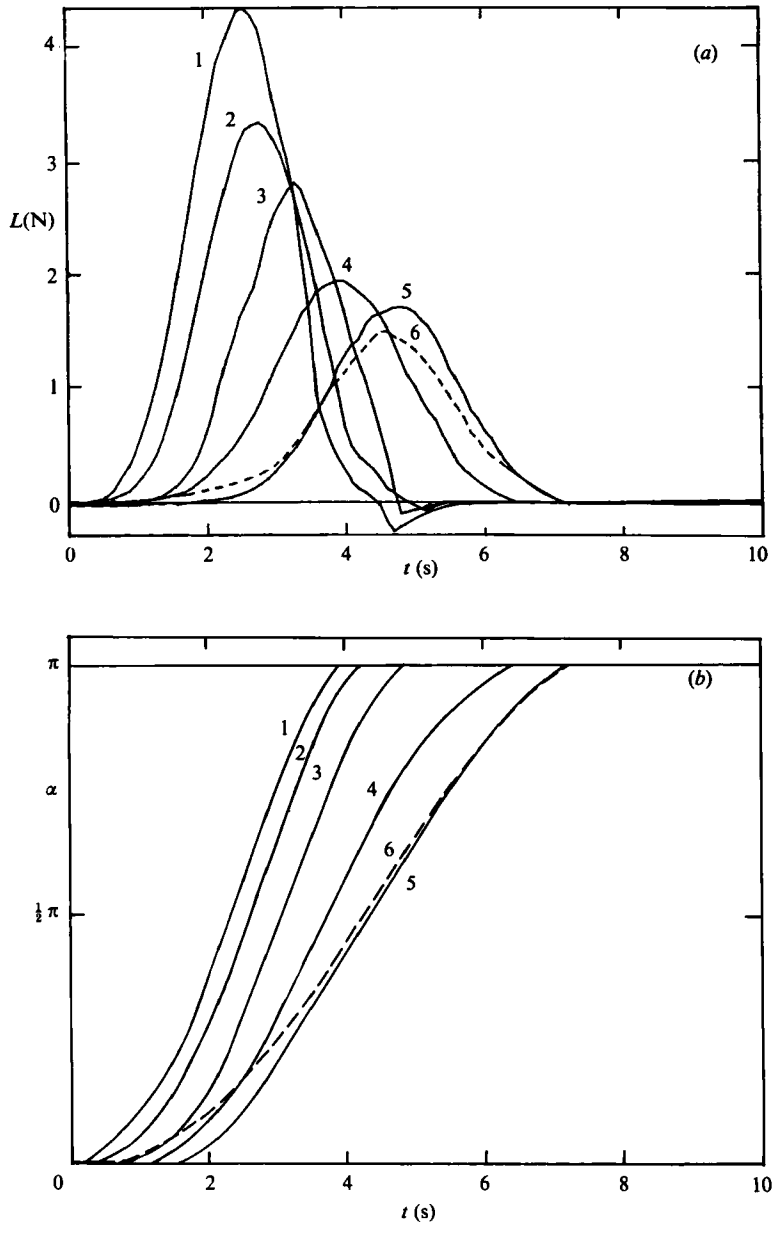

FIGURE 11 (*a–b*). For caption see facing page.

with circulation Γ and separated by a distance l then the impulse of the vortex pair is

$$I_2 = \rho \Gamma l s, \tag{6}$$

as given by Lamb (1945, §157). Figure 14 compares the two estimates for different values of W, the work done in rotating each wing through one opening cycle (π rad); so

$$W = \frac{\pi}{T} \int_0^T M(t)\, \mathrm{d}t, \tag{7}$$

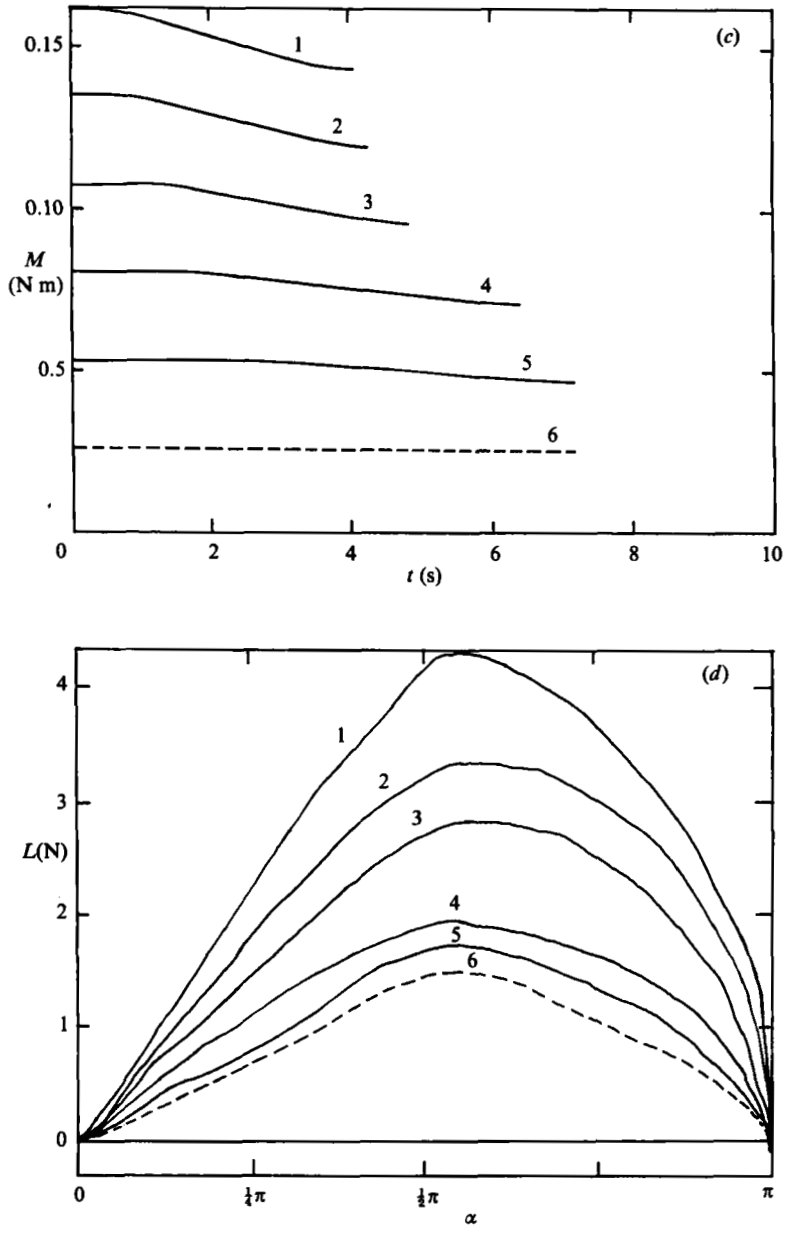

FIGURE 11. Simultaneous measurements of (*a*) $L(t)$, (*b*) $L(\alpha)$, (*c*) $M(t)$ and (*d*) $\alpha(t)$ for six different weights (traces 6–1, 5–30 g each weight, 5 g increments) used to open the wings.

where $M(t)$ is the moment applied to each wing root at time t. The agreement between the impulse derived from the $L(t)$ records (solid circles in figure 8) and that obtained from flow-visualization measurements (open circles) is fair, although the latter are consistently lower by about 15 %. A single pair of concentrated vortices is undoubtedly a simplistic modelling of the real flow field but a more realistic distribution of vorticity over some finite vortex core would decrease the calculated impulse, dropping to 0.8 of the concentrated vortex pair for a two-dimensional analogue of Hill's spherical vortex (Lamb 1945, §165). Fraenkel (1972) discusses the properties of families of

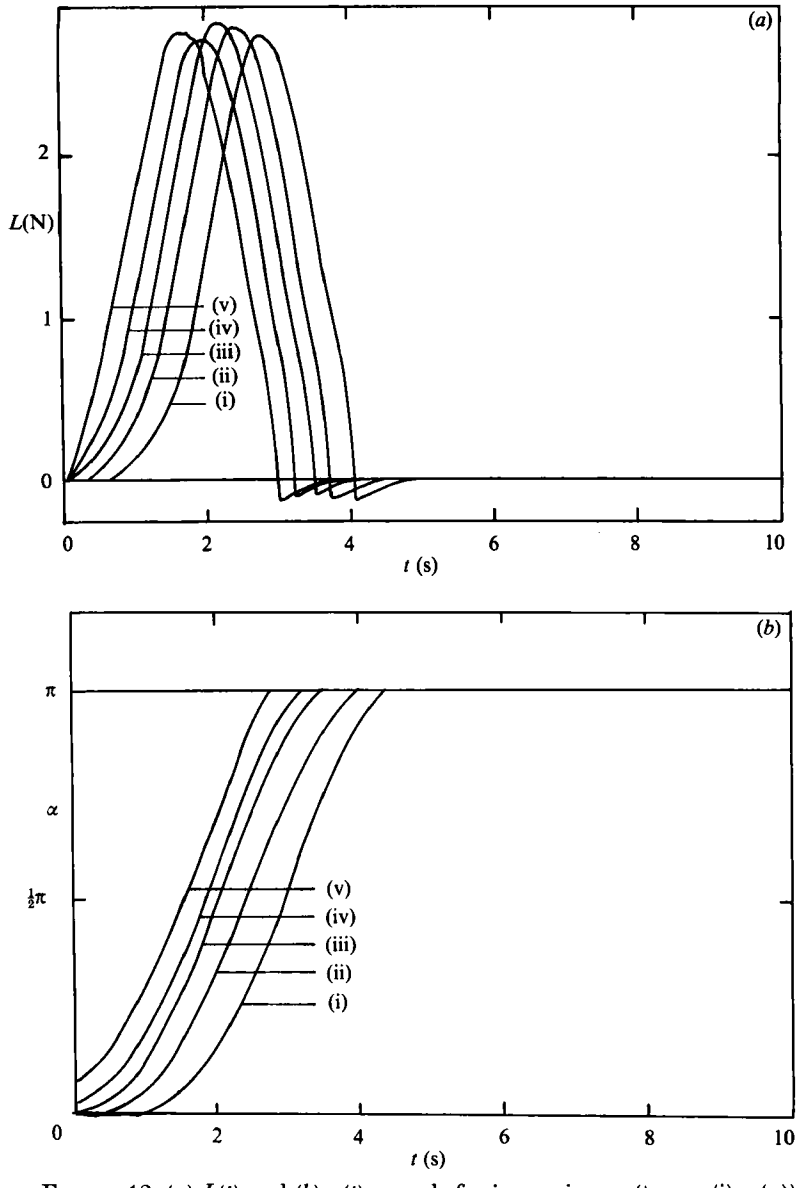

FIGURE 12. (*a*) $L(t)$ and (*b*) $\alpha(t)$ records for increasing α_0 (traces (i)→(v)).

steady vortex rings with varying core vorticity distributions. Ideally, one would measure the impulse over the entire fluid volume,

$$\boldsymbol{I} = \tfrac{1}{2}\rho \int \boldsymbol{x} \times \boldsymbol{\omega} \, \mathrm{d}V, \tag{8}$$

where $\boldsymbol{\omega}$ and $\boldsymbol{x}$ are the vorticity and position vectors of a fluid element with volume $\mathrm{d}V$. Vorticity is also generated on the lower wing surfaces as a jet of fluid is squeezed out from between the wings towards the end of the wing stroke. The impulse of this jet does not contribute towards the measured circulation as the closed-streamline technique tends to confine integral paths to circuits around the leading-edge vortices. Any extra fluid impulse due to acceleration of fluid beneath the wings was estimated

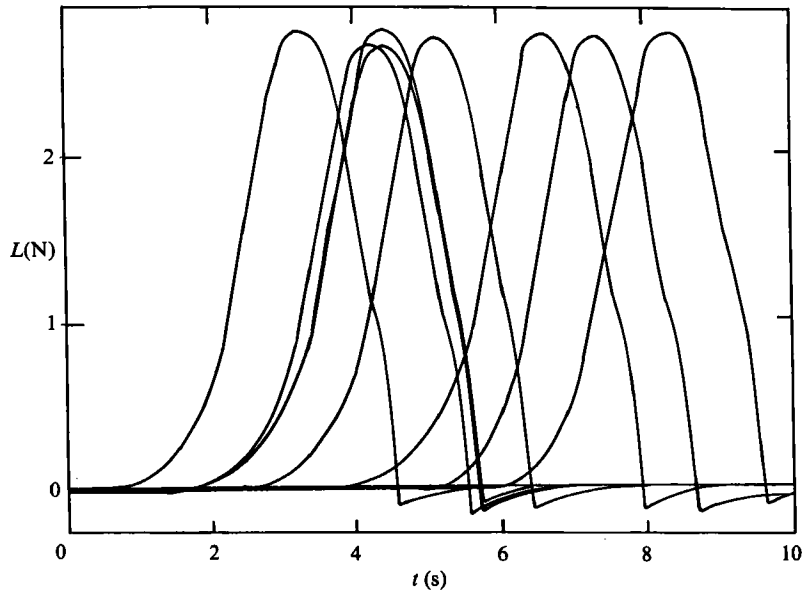

FIGURE 13. $L(t)$ traces for eight single experiments with very small α_0. Small differences in α_0 in each case produced a large spread in t.

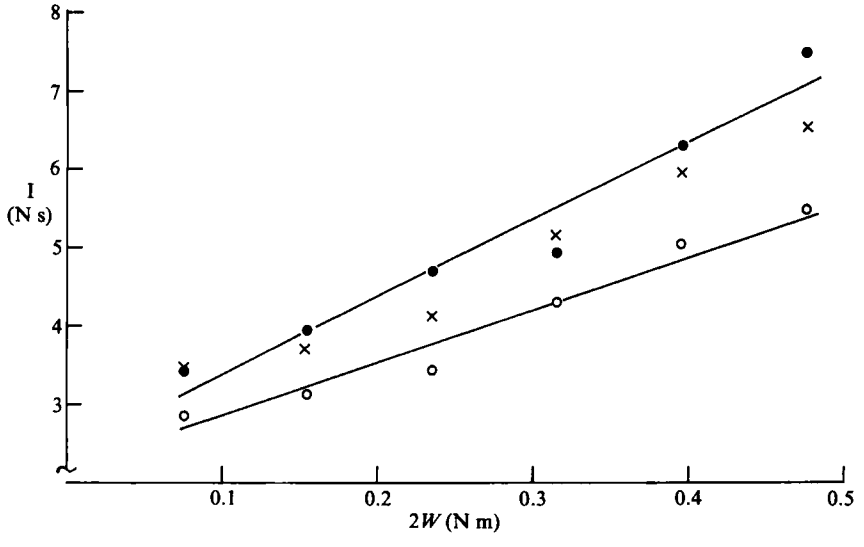

FIGURE 14. Fluid impulse calculated from $L(t)$ records (●) measured from streak photographs (○) and corrected photographic values (×), for different values of W corresponding to traces 1–6 in figure 11. Solid lines show linear regression of ● and ○ on to W.

by measuring $v(x)$ profiles across a diaphragm placed immediately beneath the wing pair. Initially, the diaphragm stretches across the entire velocity field but for $\alpha > \frac{1}{2}\pi$ it runs horizontally in a straight line from wing tip to wing tip, in an attempt to measure only those velocities due to the jet motion. This process is illustrated in figure 15. The force F_j on the wings due to acceleration of the jet was estimated from the resulting $v(x)$ velocity profiles by

$$F_j = \rho s \int_0^D v^2(x)\,\mathrm{d}x, \tag{9}$$

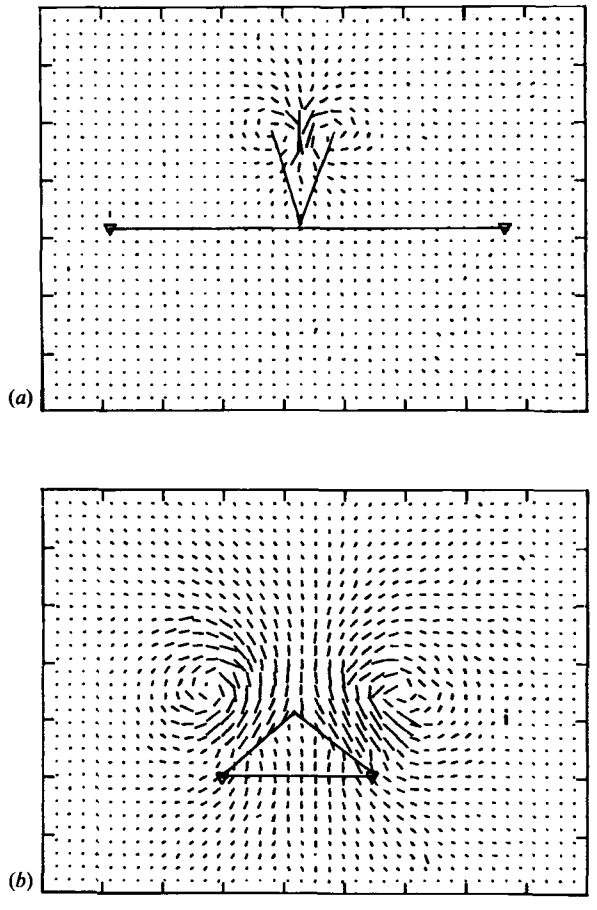

FIGURE 15. Measurement of $v(x)$ profiles for (a) $\alpha < \frac{1}{2}\pi$, and (b) $\alpha > \frac{1}{2}\pi$.

where the integral is taken across the length of the diaphragm D. The integral of this force over the wing opening time ((5)) gives the impulse of the jet-fluid motion. The division of the flow field into two separate components is again a simplification but in practice it does seem that this particular procedure for estimating the jet contribution accounts quite well for any fluid impulse missed by the circulation calculation. The crosses in figure 14 include the jet impulse and lie very close to the measured forces. The shape of a typical $L(t)$ curve should be modified as sketched in figure 16 to show the circulatory and the non-circulatory components of the lift force, and a substantial contribution from the jet impulse is evident towards the end of the wingstroke. Although the wing motions of the final phase producing the jet bear a superficial resemblance to a 'clap', the fluid dynamics are in fact quite different. The circulation on a pair of wings meeting at the end of a wingstroke would have an opposite sense of rotation. The clap motion originally envisaged by Weis-Fogh has yet to be modelled satisfactorily either theoretically or experimentally.

If $\bar{L}$ is the mean lift force on one wing over one wingstroke, we can define a mean lift coefficient,

$$\bar{C}_L = \frac{\bar{L}}{\frac{1}{2}\rho cs(\bar{\Omega}c)^2}. \tag{10}$$

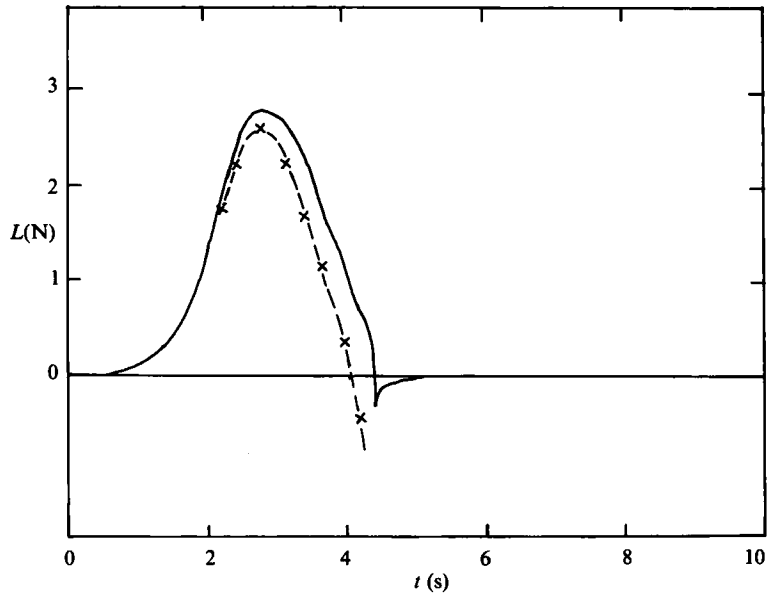

FIGURE 16. The contribution of jet momentum ot the measured $L(t)$ curves was estimated at points marked by crosses. Broken line approximates $L(t)$ history from circulatory lift.

Experiment number	Wing opening time T (s)	Mean lift force $\bar{F}$ (N)	Mean applied moment $\bar{M}$ (N m)	Total work to rotate wing W (N m)	Mean power required P (W)	Mean lift coefficient $\bar{C}_L$	Mean specific power $\bar{C}_P$	$\bar{C}_L/\bar{C}_P$
6	7.54	0.19	0.012	0.038	0.005	7.22	4.59	1.57
5	7.38	0.23	0.025	0.079	0.011	8.47	8.94	0.95
4	6.15	0.33	0.038	0.119	0.019	8.41	9.66	0.87
3	5.00	0.41	0.051	0.159	0.032	6.87	8.50	0.81
2	4.32	0.62	0.063	0.199	0.046	7.85	7.92	0.99
1	3.69	0.88	0.076	0.239	0.065	8.05	7.05	1.14

TABLE 1. Mean values are time-averaged over complete wing stroke; all measurements expressed per wing

The mean power required to open the wings is the mean rate of doing work $\overline{W}$ over the wing opening period T:

$$\bar{P} = \overline{W}/T, \tag{11}$$

and a mean power coefficient or mean specific power may be similarly defined as

$$\bar{C}_P = \frac{\bar{P}}{\frac{1}{2}\rho cs(\bar{\Omega}c)^3}. \tag{12}$$

The performance characteristics of the wings are summarized in table 1. The mean lift force $\bar{L}$ was calculated from $L(t)$ curves corrected by subtracting forces from jet propulsion (figure 16) and the $\bar{C}_L$ values in column 7 of table 1 are based on these values, reflecting the circulatory lift generation of the wing pair. Although the correct

comparison with wings in linear translation is not obvious, these values of $\bar{C}_L$ are clearly very high. The measured steady-state $C_{L\max}$ of the L1103M high-lift laminar roof-top aerofoil at $Re = 1.0 \times 10^6$ is ≈ 2.2 with the flow fully attached (Liebeck 1980). Maresca, Favier & Rebont (1979) measured time-averaged C_L values of up to 1.75, or $2\frac{1}{2}$–3 times the steady-state value for a NACA 0012 aerofoil at incidence in longitudinal oscillations parallel to the free stream for $5.7 \times 10^4 < Re < 4.0 \times 10^5$. McCroskey (1981) reports $C_{L\max} \approx 2.5$ for a Vertol VR 7 oscillating sinusoidally about the quarter-chord position at $Re \approx 1 \times 10^6$. The high unsteady lift coefficients in the latter two studies were associated with the evolution of large separation vortices at the leading edge. Here, the separation vortices remain attached to the wing surface throughout the wing rotation for all smooth wing-opening time histories. Measured $\bar{C}_L$ values of 6.9–8.5 are consistent with the value of ≈ 8.1 reported by Maxworthy (1979) for a locally two-dimensional flow over a pair of triangular wings opening in a fling up to $\alpha = \frac{1}{3}\pi$.†

The $\bar{C}_P$ measurement is a rather crude indication of the mean power required to operate the wings and varies little with mean applied moment, the exception being case no. 6 where the wings started at some small α_0 to prevent adhesion and $\bar{\Omega}$ is therefore correspondingly higher. The work W contributing to C_P includes the work required to overcome friction and inertial forces of the apparatus as well as the work done in producing the jet beneath the wings. With these considerations in mind, the small variations in $\bar{C}_P$ and $\bar{C}_L/\bar{C}_P$ for the different cases in table 1 are not thought to be significant.

6.3. *Initial opening angle* α_0

For $0.049 < \alpha_0 < 0.21$, the difference in $L(t)$ traces was not as visible in the total impulse imparted to the fluid as in the time taken to start the wings from rest. Especially at small α_0, the work done in opening the wings increases with decreasing α_0 for no measurable change in I, so the efficiency, defined as useful work done on the surrounding fluid divided by work performed in operating the wings, rises with increasing α_0 up to $\alpha_0 \approx 0.2$ rad. It is interesting to note that the small setae on the wing surface of *Encarsia formosa* would prevent complete adhesion of the wings and the various bumps and ridges (wing veins) on the wings might do the same in other insect species. For the minority of hovering insects which do use the full clap and fling (Ellington 1984), wing flexibility and the peel motion would mitigate the effects noted here for small α_0.

6.4. *Comparison with theory*

The streamlines derived from the full Navier–Stokes computation at $Re = 30$ by Haussling (1979) are qualitatively similar to those reported here and in Maxworthy (1979), although, in this case, the Reynolds number is two orders of magnitude higher and the wing motions (sinusoidal oscillations of $0 < \alpha < \frac{1}{4}\pi$ for Haussling's calculation) differ slightly. Unfortunately, circulation, pressure distribution or lift forces were not presented. Both Edwards & Cheng (1982) and Wu & Hu-Chen (1984) have calculated circulations in their separation-vortex models and these are compared with the experimental results together with the inviscid model without separation. The inviscid calculation is Lighthill's (1973) $g(\alpha)$ function, given explicitly by Edwards

† $\bar{L}$ values in table 1 may also be compared with the virtual-mass forces on a flat plate accelerating perpendicular to its chord c. The virtual mass per unit span is $\frac{1}{4}\rho\pi c^2$. If one assumes a constant acceleration $a = \mathrm{d}^2y/\mathrm{d}t^2$, the normal force $F_{\mathrm{ref}} = \frac{1}{4}\rho\pi c^2 a$. For example, in case 6, $F_{\mathrm{ref}} \approx 0.11$ N and $\bar{L}/F_{\mathrm{ref}} \approx 8$.

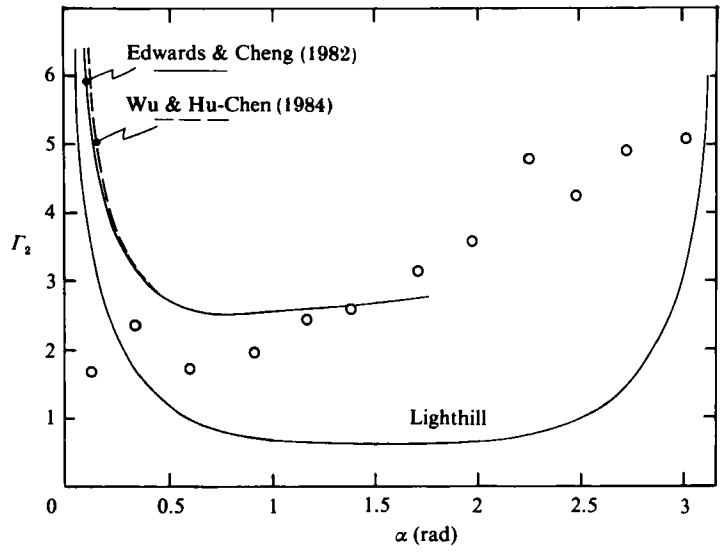

FIGURE 17. Theoretical and experimental values of the dimensionless circulation, Γ_2, normalized by the instantaneous wing angular velocity Ω.

& Cheng (1982, equation (6)). The dimensionless circulation $\Gamma_2 = \Gamma/\Omega c^2$ is plotted against α in figure 17. The Γ/c^2 values of Edwards & Cheng have been divided by Ω, where

$$\Omega = 0.5847t \text{ rad s}^{-1} \quad (t < 1.66 \text{ s}),$$

$$\Omega = 0.971 \text{ rad s}^{-1} \quad (t > 1.66 \text{ s}),$$

as given in their paper and our experimental values are divided by the measured instantaneous values of Ω. Wu & Hu-Chen's data were given in the same units as plotted here. As has been previously noted, the inviscid calculation without vortex separation does not account for the accumulation of vorticity in the fluid and Γ_2 drops from an initially infinite value to a minimum at $\alpha = \frac{1}{2}\pi$. $g(\alpha)$ is symmetrical about this point as the sink at the point of contact between the two wings behaves like a source for $\alpha > \frac{1}{2}\pi$ and fluid is expelled from between the closing wings. The experimental values of Γ_2 do not include this jet term. The agreement between experiment and the two separation-vortex models, both of which predict almost identical circulations,† is fair for $0.25 < \alpha < 1.5$, although the growth of Γ_2, which continues over the entire range of α, is quicker than predicted by theory. This may be due to the increasing divergence of the core vorticity distribution from the concentrated vortex model. Figure 18 shows isometric plots of the vorticity ω at $\alpha = 1.16$ and 2.25, measured from the streak-photograph data. The broadening of regions of high vorticity with increasing α is clear as vorticity shed at the leading edge has been convected to the edge of a core region increasing in size. Such a vorticity distribution might be more accurately modelled by the shedding and subsequent roll-up of a large number of point vortices (e.g. Moore 1974; Sarpkaya 1975); Guiraud & Zeytounian (1980) have presented an analytic solution for the inviscid core of a rolled-up vortex sheet which might be appropriate in this case.

† The close correspondence of Γ_2 calculated by the two separation-vortex models is hardly surprising as the same $\alpha(t)$ was assumed and the separation-vortex strength was increased by vorticity shed at the leading edge in both cases.

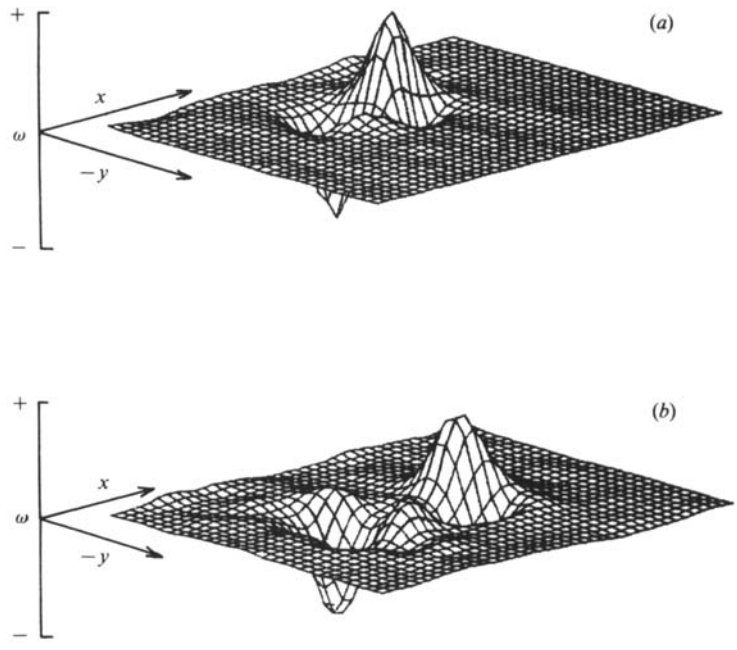

FIGURE 18. Isometric surfaces of the vorticity distribution at (a) $\alpha = 1.6$ rad, and (b) $\alpha = 2.25$ rad.

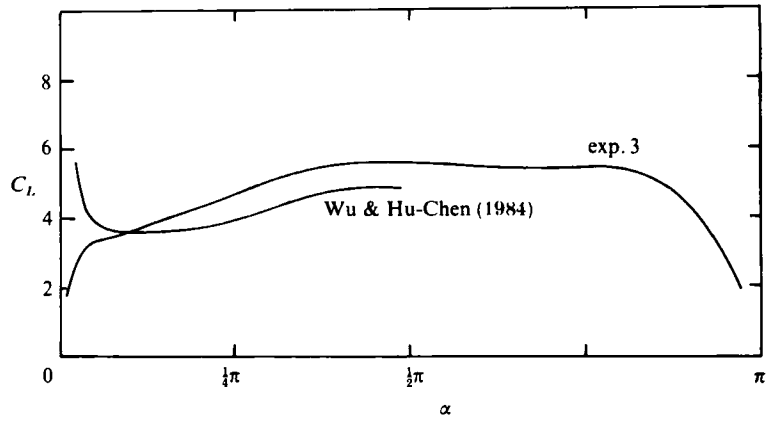

FIGURE 19. Theoretical and experimental values of $C_L(\alpha)$. Experimental points are connected by a smoothing spline curve.

Wu & Hu-Chen also calculated the lift force on the wings in the presence of separation vortices and a comparison with their data is made in figure 19. Reported values of $L/\rho c^3$, where L is the lift per unit span, are converted to a convenient dimensionless form $L/\frac{1}{2}\rho\Omega^2 c^3$, using the appropriate values of Ω, and compared with instantaneous lift coefficients, $C_L = L/\frac{1}{2}\rho cs(\Omega c)^2$, measured from one experiment corresponding to the conditions of experiment 3 of table 1, or trace 3 in figure 11 (a). The agreement between the two is close, although experimental values are consistently higher after $\alpha \approx 0.3$ rad; both demonstrate the high lift forces which may be obtained from the fling mechanism.

7. Conclusions

The two-dimensional rigid fling is capable of generating high unsteady lift forces associated with high circulations around the separation vortices. Mean lift coefficients $\bar{C}_L$, based on the mean tip velocity, of 7–8 are in general agreement with those estimated by Maxworthy (1979) for a three-dimensional clap-and-fling model, wherein simple calculations were presented to demonstrate that the available lift was more than adequate to support the weight of a hovering insect. Although the model here departs from the original clap-and-fling motion at $\alpha \approx \frac{1}{3}\pi$ (when the wings separate), the full range of $0 < \alpha < \pi$ rad might be appropriate for a two-dimensional or axisymmetric butterfly model. The rapid generation of separation vortices with high circulation and the production of correspondingly high lift forces suggests that further work on an opening-flap mechanism of vortex generation and entrapment is worth pursuing.

Certain modifications to the basic mechanism which are prevalent in nature will be simple to model on the apparatus described here with minor changes. These include the 'near' or 'partial' clap and fling, where the wings are always separated by some fraction of their chord, and also the effects of wing flexibility.

The proper control experiments for these results on an opening wing pair would involve an isolated wing in rotation, and are also feasible with only minor alterations.

It is a pleasure to thank Professor H. K. Cheng for his enthusiastic support and advice and also Dr K. Heikes who was largely responsible for the final shape of the apparatus. Thanks are also due to Dr R. Amen and to Dennis Plocher for generous help in computing affairs and to Sara Woodall for patient digitizing duties. The financial support of the National Science Foundation (Contract No. MEA-8217833) is gratefully acknowledged.

REFERENCES

DIERCKX, P. 1975 An algorithm for smoothing differentiation and integration of experimental data using spline functions. *J. Comp. Appl. Maths* **1**, 165–184.

EDWARDS, R. H. & CHENG, H. K. 1982 The separation vortex in the Weis-Fogh circulation generation mechanism. *J. Fluid Mech.* **120**, 463–473.

ELLINGTON, C. P. 1975 Non-steady-state aerodynamics of the flight of *Encarsia formosa*. In *Swimming and Flying in Nature* (ed. T. Y. Wu, C. J. Brokaw & C. Brennen), vol. 2, pp. 783–796. Plenum.

ELLINGTON, C. P. 1980 Vortices and hovering flight. In *Instationäre Effekte an schwingenden Tierflügeln* (ed. W. Nachtigall), pp. 74–101. Wiesbaden: Franz Steiner.

ELLINGTON, C. P. 1984 The aerodynamics of hovering insect flight. IV. Aerodynamic mechanisms. *Phil. Trans. R. Soc. Lond.* B **305**, 79–113.

FRAENKEL, L. E. 1972 Examples of steady vortex rings of small cross-section in an ideal fluid. *J. Fluid Mech.* **51**, 119–135.

FURBER, S. B. & FFOWCS WILLIAMS, J. E. 1979 Is the Weis-Fogh principle exploitable in turbomachinery? *J. Fluid Mech.* **94**, 519–540.

GUIRAUD, J. P. & ZEYTOUNIAN, R. KH. 1980 Rotational compressible inviscid flow with rolled vortex sheets. An analytical algorithm for the computation of the core. *J. Fluid Mech.* **101**, 393–401.

HAUSSLING, H. J. 1979 Boundary-fitted coordinates for accurate numerical solution of multibody flow problems. *J. Comp. Phys.* **30**, 107–124.

HEIKES, K. E. & MAXWORTHY, T. 1982 Observations of inertial waves in a homogeneous rotating fluid. *J. Fluid Mech.* **125**, 319–345.

IMAICHI, K. & OHMI, K. 1983 Numerical processing of flow-visualization pictures – measurement of two-dimensional vortex flow. *J. Fluid Mech.* **129**, 283–311.

LAMB, H. 1945 *Hydrodynamics.* Dover.

LIEBECK, R. H. 1980 Design of airfoils for high lift. *AIAA Paper No.* 3034.

LIGHTHILL, M. J. 1973 On the Weis-Fogh mechanism of lift generation. *J. Fluid Mech.* **60**, 1–17.

MCCLELLAN, J. H., PARKS, T. W. & RABINER, L. R. 1973 A computer program for designing optimum FIR linear phase digital filters. *IEEE Trans. Audio Electroacoust.* **21**, 506–526.

MCCROSKEY, W. J. 1981 The phenomenon of dynamic stall. *NASA TM* 81264.

MARESCA, C., FAVIER, D. & REBONT, J. 1979 Experiments on an aerofoil at high angle of incidence in longitudinal oscillations. *J. Fluid Mech.* **92**, 671–690.

MAXWORTHY, T. 1971 A simple observational technique for investigation of boundary-layers, stability and turbulence. In *Turbulence Measurements in Liquids* (ed. G. K. Paterson and J. L. Zakin). Dept Chem. Engng, University of Missouri: Rolla.

MAXWORTHY, T. 1979 Experiments on the Weis-Fogh mechanism of lift generation by insects in hovering flight. Part I. Dynamics of the 'fling'. *J. Fluid Mech.* **93**, 47–63.

MAXWORTHY, T. 1981 The fluid dynamics of insect flight. *Ann. Rev. Fluid Mech.* **13**, 329–50.

MOORE, D. W. 1974 A numerical study of the roll-up of a finite vortex sheet. *J. Fluid Mech.* **63**, 225–235.

ROSSOW, V. J. 1978 Lift enhancement by an externally trapped vortex. *J. Aircraft* **15**, 618–625.

SARPKAYA, T. 1975 An inviscid model of two-dimensional vortex shedding for transient and asymptotically steady separated flow over an inclined plate. *J. Fluid Mech.* **68**, 109–128.

SAVAS, Ö. 1985 On flow visualization using reflective flakes. *J. Fluid Mech.* **152**, 235–248.

SCHOLEY, K. D. 1982 Developments in vertebrate flight: climbing and gliding of mammals and reptiles, and the flapping flight of birds. Ph.D. Thesis, University of Bristol, England.

WAGNER, H. 1925 Über die Entstehung des dynamischen Auftriebes von Tragflügeln. *Z. angew. Math. Mech.* **5**, 17–35.

WEIS-FOGH, T. 1973 Quick estimates of flight fitness in hovering animals, including novel mechanisms for lift production. *J. Exp. Biol.* **59**, 169–230.

WU, J. C. & HU-CHEN, H. 1984 Unsteady aerodynamics of articulate lifting bodies. *AIAA Paper no.* 2184.